Asian Journal of Chemistry; Vol. 34, No. 8 (2022), 1997-2007

ASIAN JOURNAL OF CHEMISTRY

https://doi.org/10.14233/ajchem.2022.23486

Externally Silylated RH-MCM-48 from Rice Husk Silica with Superparamagnetic Iron Oxide for Multifunctional Applications

S. SUYANTA*, M. MUDASIR, W. NUGROHO and K. FAJARIATRI

Department of Chemistry, Universitas Gadjah Mada, Yogyakarta, Indonesia

*Corresponding author: Tel./Fax: +62 0274 545188; E-mail: suyanta_mipa@ugm.ac.id

Received: 17 August 2021; *Accepted*: 14 February 2022; *Published online*: 18 July 2022; AJC-20879

Rice husk silica has been used as a raw material for the sonochemical synthesis of MCM-48 (RH-MCM-48). Silylation on the outer surface of RH-MCM-48 using trimethylchlorosilane before removal of the template to prevent the formation of iron oxide in the outer of RH-MCM-48. The impregnation of Fe^{3+} into the externally silylated-RH-MCM-48 porous system was done by optimizing the concentration of Fe^{3+}, contact time and temperature. The XRD pattern, N_2 adsorption/desorption isotherms and TEM images showed that RH-MCM-48 has an ordered *Ia3d* cubic mesostructure with high specific surface area and narrow porous size distribution. FTIR spectra confirmed the successful implementation of external silylation. Moreover, DR-UV-vis spectra, EPR spectra and magnetization curve show that the impregnation of Fe^{3+} into the externally silylated-RH-MCM-48 pores produce a superparamagnetic iron oxide nanoparticles formed inside the pores and induces partial isomorphic substitution of Si^{4+} by Fe^{3+} on the wall pores.

Keywords: Iron oxide nanoparticles, MCM-48, Silylation, Impregnation, Superparamagnetic, Isomorphic substitution.

INTRODUCTION

Magnetic iron oxide nanoparticles *i.e.* Fe_3O_4 (magnetite), γ-Fe_2O_3 (maghemite) and α-Fe_2O_3 (hematite) have great potential as information storage materials [1], magnetic recyclable nano-catalysts [2], adsorbents in adsorption/separation processes [3] and applications in biomedical areas [4]. When the size of nano-particles ranging from 10 to 20 nm in diameter, magnetic nano-particles have single magnetic domains and normally show superparamagnetic behaviour at room temperature, known as superparamagnetic iron oxide nanoparticles (SPIONs) [5]. Mixed oxides of iron with certain transition metal ions such as copper, nickel, manganese, cobalt and lanthanide metals also have superparamagnetic properties and are therefore included in the SPION category. However, the most commonly used SPIONs in various biomedical applications are magnetite and maghemite nanoparticles [6] since they are relatively safer than other nanoparticles, such as manganese, which can cause neurological disorders [7] or lanthanides, which are dangerous for patients with kidney problems [8], *etc.*

The size of SPION is small enough that it behaves like a single magnetic unit, rotating in the presence of a magnetic field without remanent magnetization, which can cause agglomeration after the magnetic field is released [9]. To reduce the tendency of SPION particles to aggregate and increase their dispersibility and colloidal stability, it is necessary to apply a coating [6]. Some compounds have been used for coating the SPIONs, *i.e.* polysaccharide [10], β-cyclodextrin [11], polyethyleneimine [12], *etc.* On the other hand, silica materials especially meso-porous silica nanoparticles (MSNs) like MCM-41, MCM-48, SBA-15 and SBA-16 are the most popular matrices used as potential carriers in drug delivery system [13,14], adsorbent [15-18], catalyst [19-21], *etc.* Their advantageous properties *i.e.* well-ordered internal mesopores (usually around 2-6 nm) with large pore volume (0.6-1 cm^3/g) and surface area (700-1500 m^2/g), adjustable particle size (50-200 nm), durability, shape and easy surface modification, make them ideal plat-forms for designing multifunctional nanosystems [22-24].

Few researchers have combined those two superior materials in which SPIONs are dispersed in the pores of various hosts *e.g.* MCM-41 [25], MCM-48 [26] and SBA-15 [27,28]. However, as far as we know, there is no report dealing with the use of externally silylated MCM-48 as a host material. Silylation

on mesoporous silica nanoparticles (MSNs) has been widely reported [29,30], but is mostly not specific and carried out on the entire (inner and outer) surface of MSNs with the purpose to increase hydrophobicity and hydrothermal stability; whereas selective silylation on the outer surface of MSNs is hardly reported. In fact, three-dimensional cubic mesoporous system of MCM-48 has a larger surface area and pores volume than two-dimensional hexagonal mesoporous system of MCM-41 or SBA-15 [31]. In terms of mass transfer, MCM-48 which has a gyroidal structure is also superior to MCM-41 [32-34], therefore it is more suitable for some applications.

On the other hand, rice husks have been utilized as a source of silica in the synthesis of mesoporous silicate materials [35-37] due of its high silica content. MCM-41 produced from rice husk has been reported to have chemical and physical properties (*e.g.* crystallinity and porosity), which are not much different from those produced by commercial silica, such as tetraethyl orthosilicate (TEOS) [38]. Based on this finding, it is expected that the synthesis of mesoporous materials such as MCM-48 using rice husks as a source of silica will also be highly feasible and it is economically more profitable. Moreover, in terms of synthesis method, ultrasonic sonication has been well known to take less time and give product with the quality which is not much different than that produced by the hydrothermal method [39].

This study reports the first synthesis and characterization of superparamagnetic iron oxide in the pores of externally silylated MCM-48 (silyl-RH-MCM-48) in which MCM-48 is ultrasonically synthesized from rice husk silica. To get the optimum results, some parameters influencing the synthesis such as Fe^{3+} concentration, contact time and temperature on preserving of the host (silyl-RH-MCM-48) have been systematically optimized. The products are confirmed by FTIR, XRD, TEM, DR-UV-vis, EPR and other characterization methods. The successful external silylation on RH-MCM-48 and impregnation of iron oxide inside the pores of silyl-RH-MCM-48 is an essential achievement because it can protect the oxidation of iron oxide and therefore extend the duration of its magnetic properties.

EXPERIMENTAL

Rice husk was taken from the rice huller at Bantul District, Yogyakarta, Indonesia. Chemicals used in this study were purchased from Merck (Germany) *i.e.* H_2SO_4 (95-97%), NaOH (100%), cetyltrimethylammonium bromide (CTAB) (> 98%), trimethylchlorosilane (TMCS) (> 99%), $Fe(NO_3)_3{\cdot}9H_2O$ (≥ 98%), toluene, diethyl ether and acetone. Most of the chemicals were of analytical reagent grade and used without further purification. Distilled water was used in all experiments.

Ultrasonic emission is carried out using a Bransonic 220 ultrasonic instrument with a frequency of 48 kHz and heating power of 100 W at room temperature range of 25 to 32 ºC. X-ray diffraction (XRD) patterns were obtained at room temperature on an X-ray diffractometer Shimadzu model XD-3H, using Cu*K*α powder irradiated at λ = 0.15418 nm. Fourier-transform infrared (FTIR) spectroscopic analysis was carried out by a Shimadzu FTIR-8010PC and the spectra were recorded as the transmittance mode in the range of 4000-400 cm^{-1} at room temperature using the KBr disc. The Nova 1200 Quantachrome of gas adsorption analyzer (GAA) was used to measure the nitrogen adsorption-desorption isotherm at liquid nitrogen temperature. Before measurement, samples were outgassed at 250 ºC overnight. The Brunauer-Emmett-Teller (BET) surface area is determined based on the multipoint BET method by utilizing adsorption data at a relative pressure (P/P_o) of 0.05-0.30. Mesoporous volume was obtained from isotherms at a relative pressure of 0.95. The estimation of average mesoporous diameter was based on the nitrogen isotherm adsorption branch using the Barrett-Joyner-Helenda (BJH) method. The BJH model was used to obtain the pore size distributions. The features of the MCM-48 pores were observed using transmission electronic microscopy (TEM) JEM-3010. Electron paramagnetic resonance (EPR) JEOL spectrometer type JES R1X was used to characterize the oxidation states of iron, while diffuse reflectance ultraviolet-visible (DR-UV-Vis) UV 1700 Pharmaspec was used to characterize the isolated iron in the framework materials. The magnetic properties of the samples were analyzed using a vibrating sample magnetometer (VSM) Oxford 1.2H with magnetic fields of up to 3T at room temperature. The iron content of the loaded samples was determined by Atomic Absorption Spectrometry (AAS-3300 Perkin-Elmer).

General procedure

Extraction of silica from rice husk: Amorphous silica was extracted from rice husk ash by modifying the procedures reported in previous literature [35,36]. The rice husk ash was obtained from the dried and cleaned rice husk burning in the open air. The obtained rice husk ash (100 g) was refluxed with H_2SO_4 solution (2 M, 500 mL) under magnetic stirring at 80 ºC for 4 h. The solid phase was separated by filtering, then washed thrice with distilled water to remove excess H_2SO_4. Afterward, the solid phase was heated at 110 ºC for 10 h followed by calcination at 600 ºC for 6 h with the heating rate of 2 ºC/min.

Synthesis of MCM-48 and its silylation: MCM-48 was synthesized according to reported procedure [31] with some modifications. Firstly, solution A and solution B were prepared. To make solution A, RH-silica (4.00 g) and NaOH (1.25 g) were added to distilled water (35 mL) then heated (80 °C) while stirring constantly for 2 h. The solution was then cooled to room temperature. Solution B was prepared by dissolving CTAB (5.04 g) in distilled water (55 mL) while simultaneously heating at 80 ºC and continously stirring for 2 h. The surfactant solution of CTAB was then cooled to room temperature. The two solutions (A and B) were mixed under vigorous stirring for 2 h, then the mixture was adjusted to pH 10 by dropwise addition of 0.1 M H_2SO_4 to produce silica-surfactant gel. The obtained gel was then placed in the ultrasound-assisted reaction apparatus, in a sealed glass bottle for 3 h at the frequency of 40 Hz and preserved at room temperature. The obtained product was recovered by filtration, washed repeatedly with distilled water and then dried at 110 ºC for 6 h. The product was denoted as as-RH-MCM-48. A portion of as-RH-MCM-48 was then calcined at 550 ºC for 5 h to produce calcined MCM-48 (cal-RH-MCM-48), while the other sample was subjected to further treatment to yield silyl-RH-MCM-48. Silylation was conducted

in accordance with the procedure described in the literature [29]. The as-RH-MCM-48 (1 g) was put into a 100 mL round bottom flask, then 50 mL of TMCS/toluene solution (10 vol. %) was added along with stirring at room temperature for 6 h. The product was filtered and rinsed with diethyl ether followed by acetone and then dried in a vacuum oven at 50 ºC for 8 h. The sample was then calcined at 550 ºC for 5 h to give silyl-RH-MCM-48.

Impregnation of Fe^{3+} into silyl-RH-MCM-48: Before impregnation, silyl-RH-MCM-48 was first activated at 120 ºC for 3 h. Next, 100 mL of acidic solutions (pH = 1) of 0.01 M $Fe(NO_3)_3$ was added dropwise into the beaker glass containing 1 g of silyl-RH-MCM-48. The mixture was then magnetically stirred for 2 h at room temperature, followed by incubation for 5 h to maximize the loading. The solid phase was filtered, washed with distilled water and dried at room temperature. To ensure the formation of iron oxide nanoparticles, the loaded sample was calcined at 500 ºC in air for 8 h. The effect of Fe^{3+} various concentrations (0.01, 0.05, 0.1, 0.25, 0.75 and 1 M), contact times (2, 4, 6, 8 and 10 h) and mixing temperatures (room temperature (room temperature, 40, 60 and 80 ºC) on the effectiveness of impregnation were also investigated in these experiments. The final product was denoted as Fe_2O_3(x,y,z)@ silyl-RH-MCM-48, where x, y and z referred to Fe^{3+} molar concentration, contact time and temperature, respectively.

The preservation/stability of host material was studied by the XRD method, while the content of Fe in the composites was determined by the AAS method. The optimal/best product was further characterized by using FTIR, DR-UV-visible, EPR and VSM methods. Fig. 1 gives the schematic illustration of the external silylation of RH-MCM-48 and the impregnation of Fe^{3+} into the pores of silylated RH-MCM-48.

RESULTS AND DISCUSSION

XRD studies: The X-ray diffractogram of as-RH-MCM-48, cal-RH-MCM-48 and silyl-RH-MCM-48 are shown in Fig. 2. The as-RH-MCM-48 sample (Fig. 2a) shows an intense peak at 2θ = 2.47º due to [211] plane and a weak peak at 2θ = 4.51º due to [232] plane; whereas cal-RH-MCM-48 sample (Fig. 2b) exhibits an intense peak at 2θ = 2.74º due to [211] plane, a weak shoulder peak at 2θ = 2.98º due to [220] plane and a weak peak at 2θ = 4.71º due to the [232] plane. These peaks matched well with the characteristic *Ia*3*d* cubic mesophase structure and resemble the same as that of conventional siliceous MCM-48 [40]. The calcination caused an increase in the peak intensity of [211] plane approximately 2 times compared to the previous one.

This change in peak intensity is caused by the significantly improved diffraction contrast between the pores and the framework after the removal of the surfactant template. In addition,

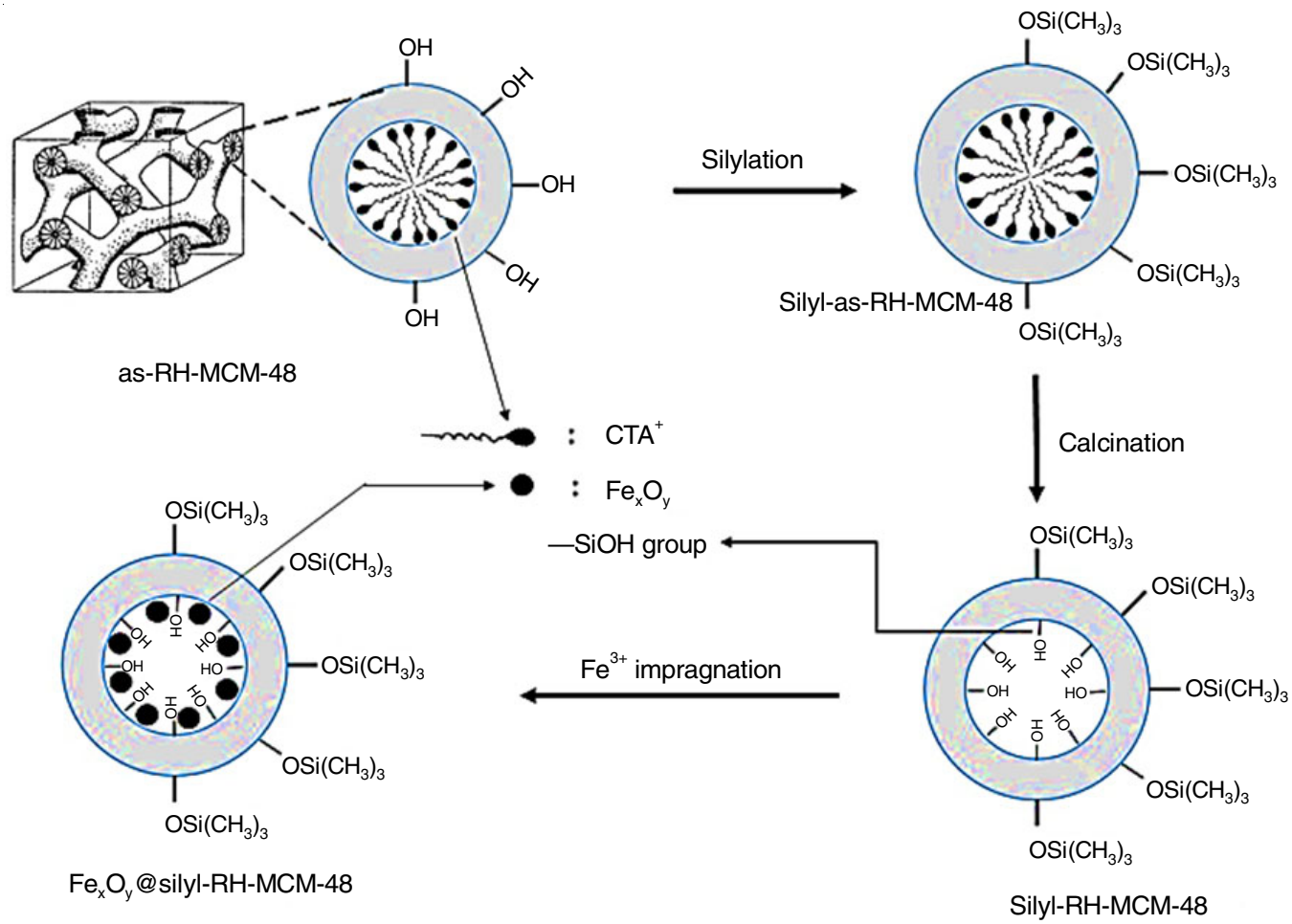

Fig. 1. Schematic illustration of external silylation of RH-MCM-48 and the impregnation of Fe^{3+} into its pores

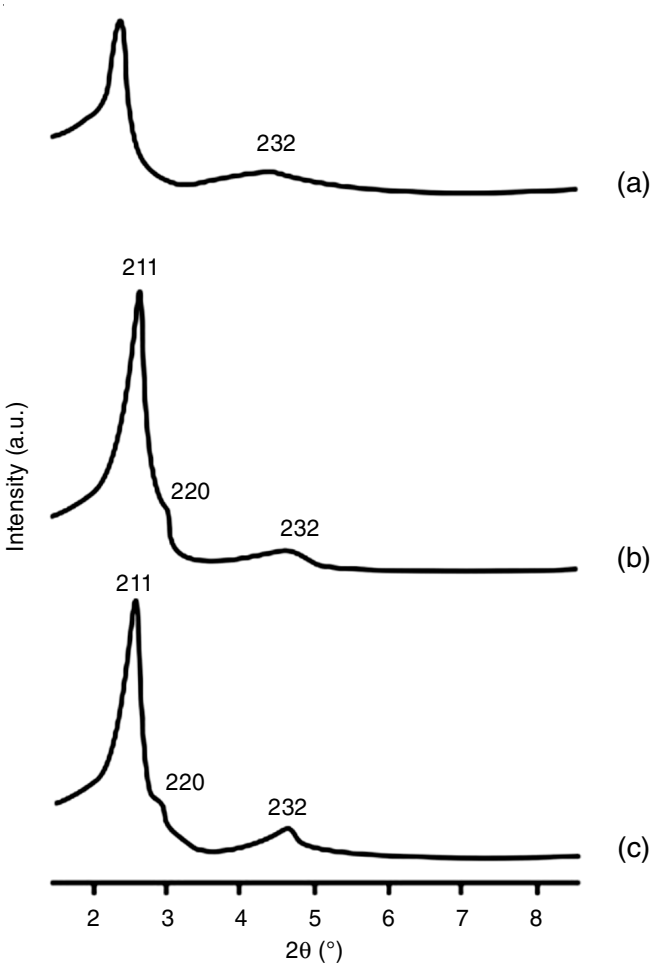

Fig. 2. X-ray diffractogram of as-RH-MCM-48 (a), cal-RH-MCM-48 (b) and silyl-RH-MCM-48 (c)

the peak of [211] shifts to the larger wavelength (from 2.47º to 2.74º 2θ), indicating that the removal of surfactant template causes the decrease in unit cell volume. For silyl-RH-MCM-48 sample (Fig. 2c), the intensity of all the peaks almost equal to that of calcined-RH-MCM-48. This is easily understood as the silylation does not occur in the internal surface so that the scattering contrast is not affected and remain the same. In addition, there is no significant difference in the position of the peaks between cal-RH-MCM-48 and silyl-RH-MCM-48, suggested that the silylation does not cause structural changes in RH-MCM-48 sample.

The X-ray diffractogram patterns of Fe_2O_3(x)(2h)(rt)@ silyl-RH-MCM-48 samples resulted from Fe^{3+} impregnation with various Fe^{3+} concentrations are presented in Fig. 3. For comparison, the diffractogram of silyl-RH-MCM-48 was also shown. The intensity of the [211] peak decreases along with the increase in Fe^{3+} concentration. This is probably attributed to the reduction of scattering contrast between the pores and the framework of the mesoporous materials due to the incorporation of Fe_2O_3 nanoparticles in the pores [41]. In general, the insertion of material into the pore results in the increase of the mutually cancelling phase between the one which is scattered by the wall and the other which is dissipated by the pore. Ultimately this reduces the intensity of scattering on the Bragg reflection.

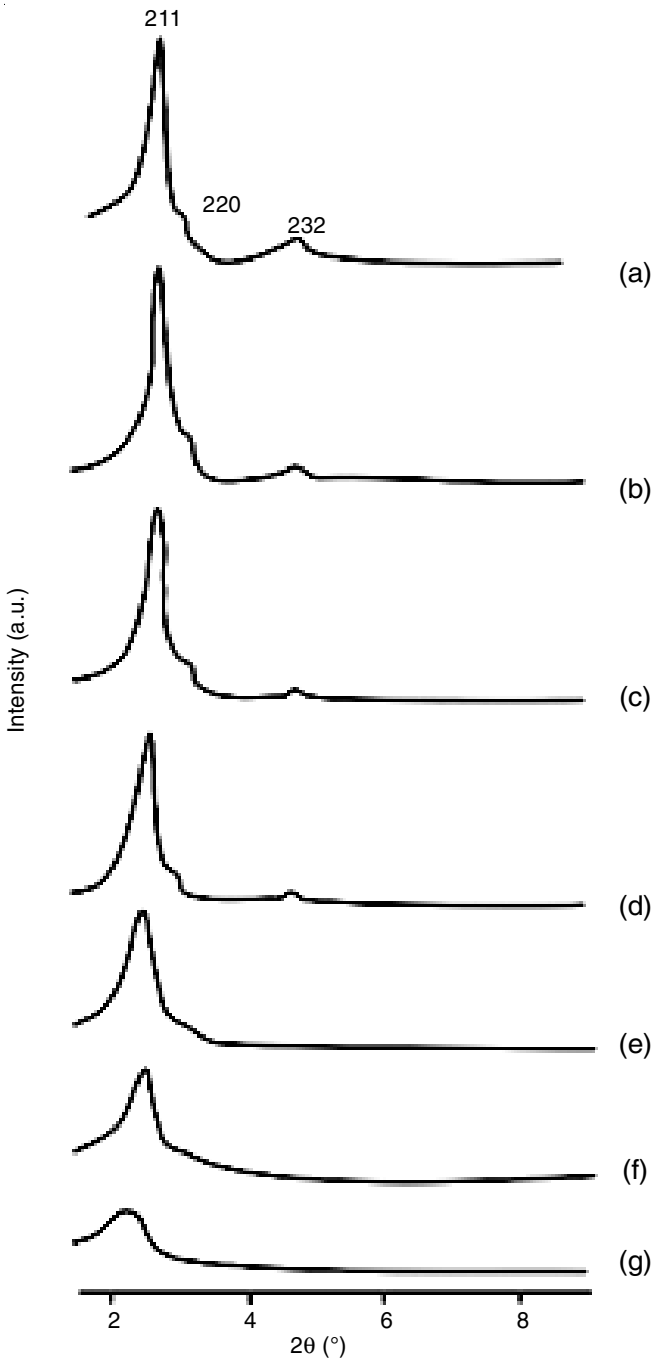

Fig. 3. Diffractogram of silyl-RH-MCM-48 (a) and Fe_2O_3(x)(2h)(rt)@silyl-RH-MCM-48 with various Fe^{3+} concentrations: 0.01, 0.05, 0.10, 0.25, 0.75 and 1 M (b-g)

The formation of iron oxide nanoparticles in the pores of silyl-RH-MCM-48 is believed to be initiated by the formation of hydrogen bonds between the silanol groups on the internal surface of silyl-RH-MCM-48 and the hydrated ligands in the Fe(III) cation such as two-core cation $Fe_2(OH)_2(H_2O)_8^{4+}$, which is present in quite abundant amounts in a solution of Fe(III) at low pH [42]. During the filtering, washing and calcination processes, there was a significant increase in the concentration of $Fe_2(OH)_2(H_2O)_8^{4+}$ so that it reached a supersaturated state and precipitated to produce iron oxide nanoparticles. This proposed mechanism (Fig. 4) can explain the non-formation

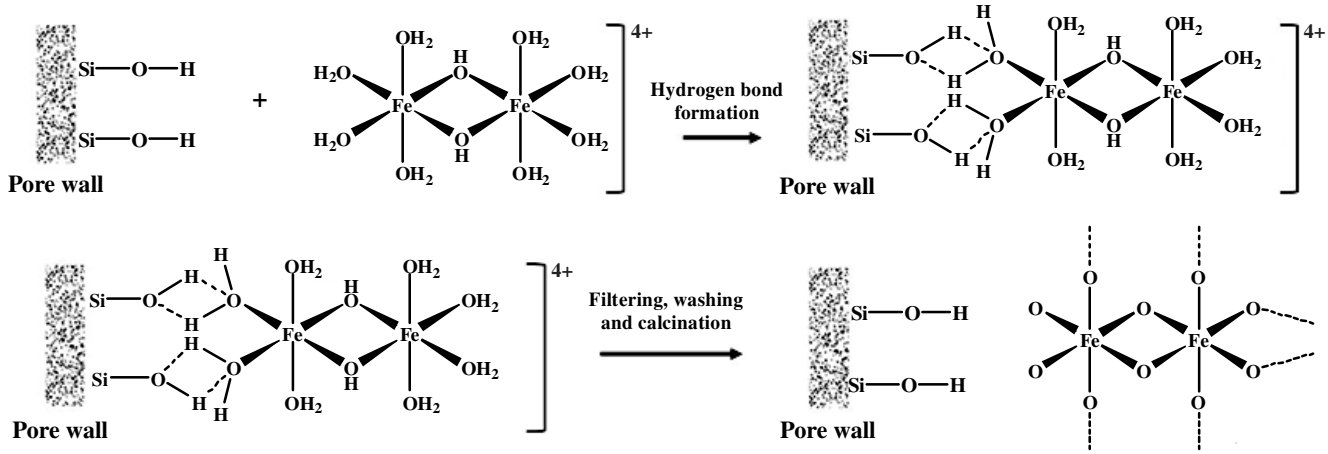

Fig. 4. Mechanism of iron oxide nanoparticles formation in the silyl-RH-MCM-48 pores

of iron oxides on the outer surface of silyl-RH-MCM-48 where the silanol groups have been deactivated with the trimethylsilyl groups.

Compared with silyl-RH-MCM-48, all peaks corresponding to Fe_2O_3(x)(2h)(rt)@silyl-RH-MCM-48 shift evidently to the smaller diffraction angle (2θ), suggesting an increase in the unit cell parameter (a_0), which may be attributed to the isomorphic substitution in which Si^{4+} (Pauling radius = 42 pm) is replaced by Fe^{3+} (Pauling radius = 64 pm) [43]. A schematic illustration for isomorphic substitution of Si^{4+} by Fe^{3+} is shown in Fig. 5, which showed that at the end, Fe is negatively charged that can undergo protonation and acted as a Brønsted acid, which has catalytic properties.

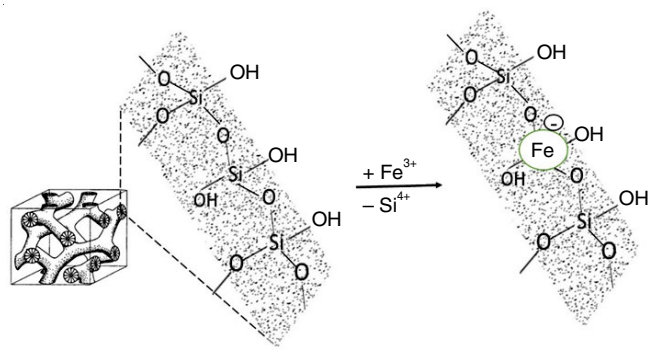

Fig. 5. Schematic illustration for isomorphic substitution of Si^{4+} by Fe^{3+}

When the concentration of Fe^{3+} is relatively small, namely 0.01, 0.05 and 0.1 M, the peaks of the [211] plane is still quite sharp even though their intensity decreases. This suggest that the cubic structure of silyl-RH-MCM-48 is preserved. On contrary, when the concentration of $Fe^{3+} \geq 0.25$ M; a small intensity and broad peaks are observed, indicating a breakdown in the cubic structure. Similar results were also reported by several researchers [44,45]. The structural damage is probably due to excessive replacement of Si^{4+} by a larger ion size of Fe^{3+}. The content of Fe in Fe_2O_3(x)(2h)(rt)@silyl-RH-MCM-48 samples (Table-1) shows that the weight % of Fe increases with the increasing Fe^{3+} concentration in the precursor solution. The maximum Fe content without causing damage to the silyl-RH-MCM-48 structure in this study is 2.43 wt.%, *i.e.* when the solution of Fe^{3+} 0.1M was used. This condition has been selected for further study.

TABLE-1
EFFECT OF [Fe^{3+}] IN PRECURSOR SOLUTION ON THE Fe CONTENT IN THE SAMPLE

Sample code	[Fe^{3+}] (M)	Fe content (wt.%)
Fe_2O_3(0.01M,2h,rt)@silyl-RH-MCM-48	0.01	1.13
Fe_2O_3(0.05 M,2h,rt)@silyl-RH-MCM-48	0.05	2.21
Fe_2O_3(0.10M,2h,rt)@silyl-RH-MCM-48	0.10	2.43
Fe_2O_3(0.25 M,2h,rt)@silyl-RH-MCM-48	0.25	2.96
Fe_2O_3(0.75 M,2h,rt)@silyl-RH-MCM-48	0.75	3.64
Fe_2O_3(1.00 M,2h,rt)@silyl-RH-MCM-48	1.00	4.28

There is no additional specific diffraction of crystalline peaks in the wide-angle region (not shown here), indicating the absence of bulky iron oxide and/or oxyhydroxides aggregates on the outer surface of the materials. Meanwhile, the existence of iron oxide nanoparticles formed in the pore system of silyl-RH-MCM-48 are too small to be detected by X-ray diffraction. Thus, the deactivation of external silanol groups by trimethylchlorosilane (TMCS) has succsessfully arranged Fe^{3+} ions into the pores and prevented the formation of bulky iron oxide and/or oxyhydroxides on the outer surface.

Fig. 6 presents the effect of contact time of impregnation on the X-ray diffractogram patterns for the sample of Fe_2O_3 (0.1M,y,rt)@silyl-RH-MCM-48. It is observed that the XRD peak intensity only slightly decreases with increasing contact time up to 10 h. This indicates that the cubic structure of silyl-RH-MCM-48 was still preserved and the contact time of up to 10 h does not cause any serious damage to the host structure. The Fe content in the silyl-RH-MCM-48 host (Table-2) shows a slight increase in the contact time of 2 to 4 h, but after that, it is almost constant. This indicates that a contact time of 4 h is sufficient for impregnation and was selected for further study.

Fig. 7 shows the XRD diffractogram pattern of Fe_2O_3 (0.1M,4h,z)@silyl-RH-MCM-48 at various temperatures. Increasing the temperature up to 60 ºC does not cause a significant reduction in peak intensity of the diffractogram. However, at 80 ºC and especially at 100 ºC, a significant reduction in the

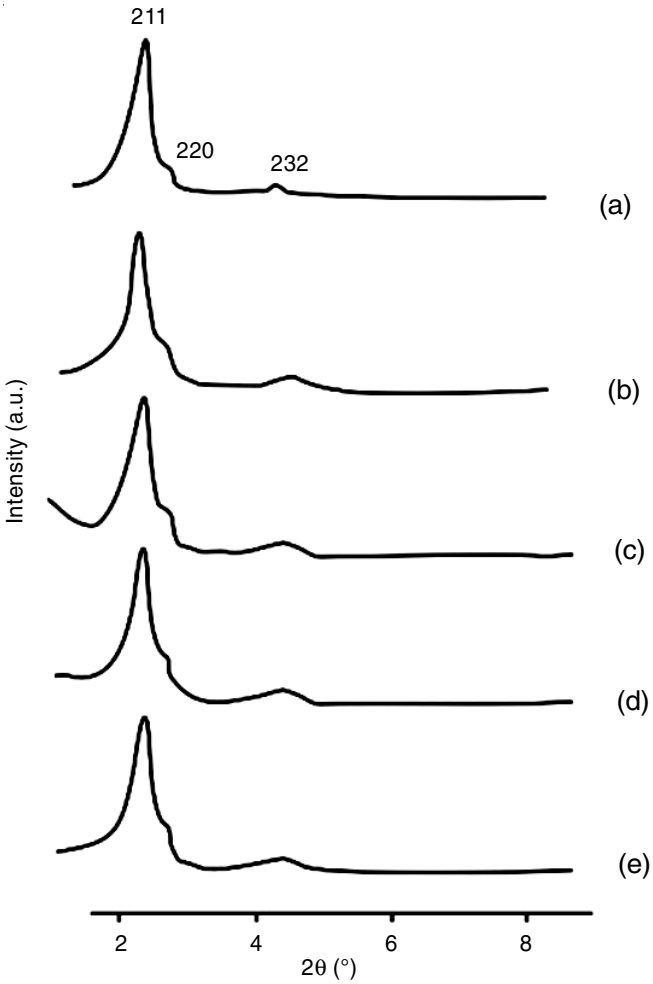

Fig. 6. X-ray diffractogram of Fe_2O_3(0.1M)(y)(rt)@silyl-RH-MCM-48 with various of contact time: 2, 4, 6, 8 and 10 h (a-e)

TABLE-2
EFFECT OF CONTACT TIME ON THE Fe CONTENT
IN Fe_2O_3(0.10M,y,rt)@silyl-RH-MCM-48 SAMPLE

Sample code	Contact time (h)	Fe content (wt.%)
Fe_2O_3(0.10M,2h,rt)@silyl-RH-MCM-48	2	2.43
Fe_2O_3(0.10M,4h,rt)@silyl-RH-MCM-48	4	2.68
Fe_2O_3(0.10M,6h,rt)@silyl-RH-MCM-48	6	2.69
Fe_2O_3(0.10M,8h,rt)@silyl-RH-MCM-48	8	2.73
Fe_2O_3(0.10M,10h,rt)@silyl-RH-MCM-48	10	2.75

intensity of the [211] peak is clearly observed; indicating the existence of structural breakdown of the silyl-RH-MCM-48.

This phenomenon suggests the poor hydrothermal stability of silyl-RH-MCM-48, which may be caused by the fact that external silylation on RH-MCM-48 is not sufficient to increase the hydrothermal stability. Some researchers [46,47] reported that silylation of mesoporous silicates is able to increase the hydrothermal stability significantly, however it should be noted that the silylation carried out by previous researchers was done on the whole materials, *e.g.* both outer and inner surfaces. While in present experimental work, silylation was carried out only on the outer surface. The outer surface of the mesoporous material contributes only a small part (about 15%) to the total surface, while the rest (about 85%) is the internal surface [48].

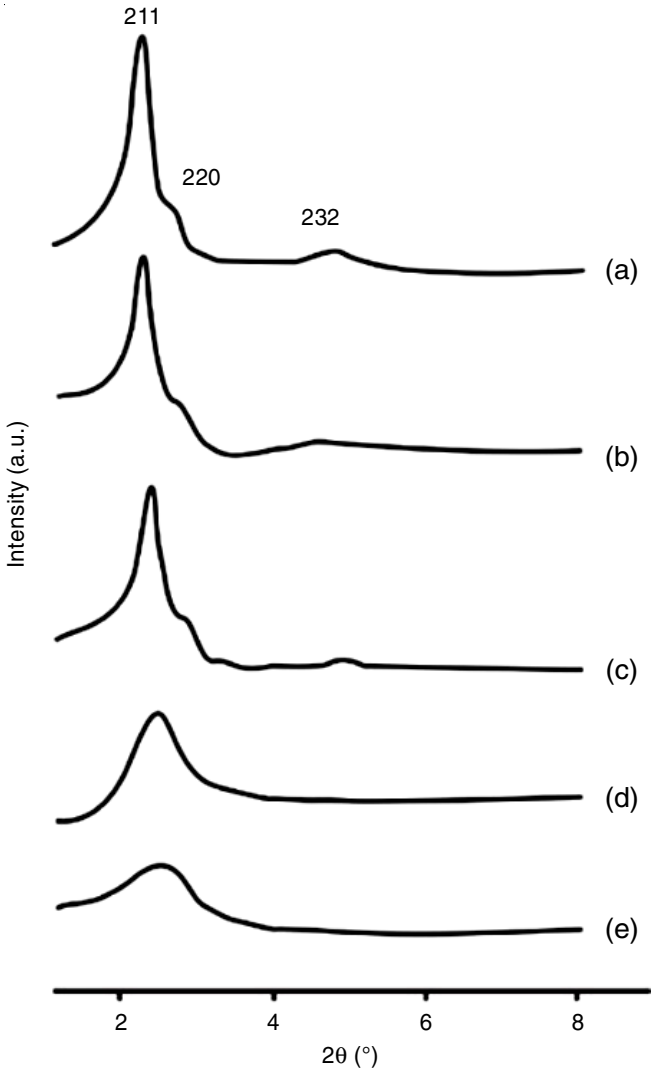

Fig. 7. X-ray diffractogram of Fe_2O_3(0.1M,4h,z)@silyl-RH-MCM-48 with various temperature: rt, 40, 60, 80 and 100 °C (a-e)

Therefore, it is not surprising that the silylation of RH-MCM-48 in present study does not increase its hydrothermal stability significantly. The rapture of mesoporous structure by hydrolysis is believed to be caused by a break of siloxane bridge to produce silanol groups in accordance with the following reaction [49]:

$$\equiv Si\text{-}O\text{-}Si\equiv + H\text{-}O\text{-}H \longrightarrow \equiv Si\text{-}OH + HO\text{-}Si\equiv \quad (1)$$

Table-3 shows the effect of impregnation temperature on the iron content in the sample. Up to 60 ºC, the Fe content increases with the increase in temperature. At higher temperatures (60 ºC), the effectiveness of collisions between the reactant particles increases, so that more iron oxide nanoparticles are formed in the pores and more Fe replaces Si in the framework. The Fe content is relatively constant when the temperature was raised up to 100 ºC. The constant level of Fe content with the increase of temperature indicates that the lower [211] peak intensity (Fig. 7c-d) is caused by the structural damage due to temperature increases and not caused by reducing of scattering contrast between the pores and the framework due to the more filling of the pore. Based on this result, the temperature 60 ºC was selected as the optimal temperature for impregnation.

TABLE-3
EFFECT OF TEMPERATURE ON
THE Fe CONTENT IN THE SAMPLE

Sample code	Temp. (°C)	Fe content (wt.%)
Fe_2O_3(0.10M,4h,rt)@silyl-RH-MCM-48	RT	2.68
Fe_2O_3(0.10M,4h,40)@silyl-RH-MCM-48	40	2.82
Fe_2O_3(0.10M,4h,60)@silyl-RH-MCM-48	60	2.96
Fe_2O_3(0.10M,4h,80)@silyl-RH-MCM-48	80	2.98
Fe_2O_3(0.10M,4h,100)@silyl-RH-MCM-48	100	2.95

FTIR studies: The FTIR spectra of as-RH-MCM-48, cal-RH-MCM-48, silyl-RH-MCM-48 and Fe_2O_3(0.10M,4h,60 ºC) @silyl-RH-MCM-48 are presented in Fig. 8. All curves exhibit the strong broaden peak near 3470 cm^{-1} related to OH asymmetric stretching vibration absorption of silanol groups and adsorbed water molecules. Additionally, the peak near 949 cm^{-1} is attributed to –OH bending vibration of surface hydroxyl groups [50]. Due to the emerging of internal silanol groups after calcination, the intensity of 3470 cm^{-1} and 949 cm^{-1} peaks in Fig. 8b is stronger than that of Fig. 8a. A broad high-intensity absorption peak of 1080 cm^{-1} corresponds to the Si–O–Si bond symmetric stretching vibration of MCM-48 skeleton, whereas the 1650 cm^{-1} absorption peak corresponds to the bending vibration of adsorbed water (–OH groups are hydrophilic). The band at 802 cm^{-1} is associated with symmetric Si-O-Si stretching, whereas the band at 468 cm^{-1} is assigned to a SiO_4 bending mode [51].

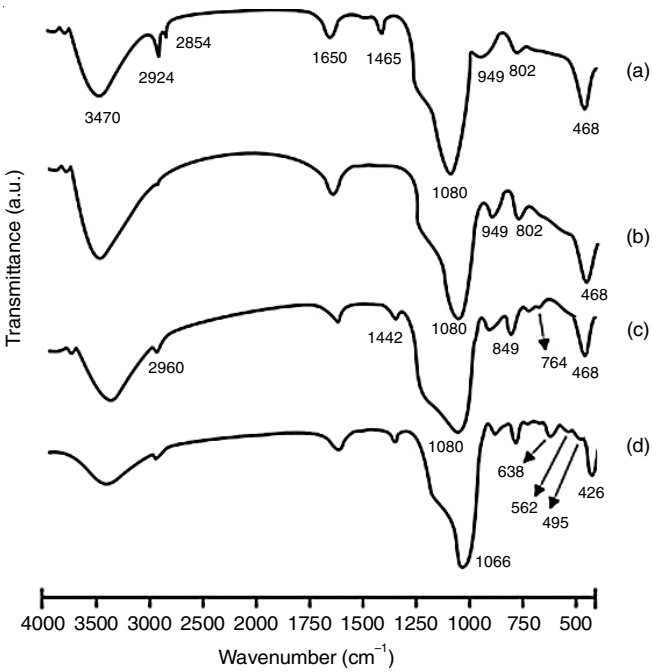

Fig. 8. FTIR spectra of as-RH-MCM-48 (a), cal-RH-MCM-48 (b) and silyl-RH-MCM-48 (c) and Fe_2O_3(0.10M,4h,60ºC)@silyl-RH-MCM-48 (d)

The IR spectrum (Fig. 8a) has several absorption peaks originating from the surfactant functional group, *i.e.* $CTMA^+$. Peaks at the wavenumber 2924 and 2854 cm^{-1} related to the asymmetric and symmetric stretching vibration of $–CH_3$, respectively [47]. The peak around 1465 cm^{-1} appears from the scissoring vibration of $–CH_2–$ and asymmetries bending vibration of CH_3-N^+ group [47]. In Fig. 8b, no peak related to the existence of $CTMA^+$ is observed, which indicates the complete removal of surfactant by calcination treatment.

The spectrum of Fig. 8c shows the peaks at 2960 and 1442 cm^{-1}, associated with the asymmetric bending and C-H stretching of methyl (-CH_3) groups produced by the silylation process, respectively [52]. At the same time, the reduction in peak intensity of the symmetrical strain of Si-OH is observed at 3436 and 949 cm^{-1}. Also, the weak peaks emerged at 849 and 764 cm^{-1}, which is the characteristics of Si-C rocking and stretching vibrations, respectively [52]. The success of silylation can also be proven by comparing a coefficient (R) for silylated and unsilylated samples, where R is defined to represent the ratio between the peak intensity of the Si-OH bond at around 949 cm^{-1} and that of the Si-O-Si bond at around 1080 cm^{-1} in the same spectrum. As shown in Fig. 8, the R of Fig. 8c is smaller than Fig. 8b, indicating that H in the silanol group on the outer surface has been replaced by the trimethylsilyl (TMS) group. These results suggested that the $–Si(CH_3)_3$ groups have successfully grafted on the outer surface of RH-MCM-48.

The spectrum (Fig. 8c) still has a peak of the Si-OH bond, because the silylation was carried out only on the outer surface. The reaction of silylation can be illustrated as [29]:

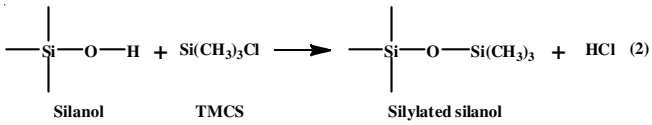

This external silylation is expected to improve the steric hindrance of the outer surface and prevent the formation of agglomerated iron oxides.

The weak peaks at 638 and 562 cm^{-1} are related to Fe-O-Fe vibration of γ-Fe_2O_3 [53] positioned in the pore of MCM-48, while the weak peak at 495 cm^{-1} is associated with Fe(III)-O-Si bending mode vibration [54] in the MCM-48 framework (Fig. 8d). Consistent with this interpretation, the band at 1080 cm^{-1} is due to the strain vibration of Si-O-Si group shifts to 1066 cm^{-1}. This is probably caused by the replacement of Si in the skeleton by Fe, leading to the formation of Si-O-Fe bond with higher reduced mass. In addition, as a secondary effect the band at 468 cm^{-1} which is attributed to SiO_4 bending mode shifts to 426 cm^{-1}. The other characteristic peak of Fe-O bonds is observed at 450 cm^{-1} and assigned to Fe–O stretching mode [55]. This peak is overlapped with the peak of Si-O bending vibration at 426 cm^{-1}. Thus, the FTIR characterization has clearly indicated the formation of iron oxide nanoparticles in the pore of MCM-48 as well as the occurrence of isomorphic substitution of Si in the pore wall by Fe. The iron(III) salt is fully decomposed, as indicated by the absence of a characteristic infrared peak of nitrate at 1380 cm^{-1}.

Surface area: Fig. 9 shows the N_2 sorption isotherms of cal-RH-MCM-48, silyl-RH-MCM-48 and Fe_2O_3(0.10M,4h, 60ºC)@silyl-RH-MCM-48 along with the corresponding pore size distribution curves calculated from the adsorption branch by the BJH method. The BET surface area, total pore volume and pore diameters values of these materials are listed in Table-4. There is no significant difference between the isotherm of

TABLE-4
POROSITY OF cal-RH-MCM-48, silyl-RH-MCM-48 AND Fe_2O_3(0.10M,4h,60°C)@silyl-RH-MCM-48

Sample	S_{BET} [(a)] (m^2/g)	V_p [(b)] (10^{-6} m^3/g)	d_pBJH [(c)] (nm)
cal-RH-MCM-48	984.28	0.763	2.589
silyl-RH-MCM-48	982.81	0.724	2.414
Fe_2O_3(0.10M,4h,60°C)@silyl-RH-MCM-48	932.32	0.495	2.066

[a]BET surface area was estimated by multipoint BET method using the adsorption data in the range of P/P_o = 0.05-0.30; [b]Total pore-volume calculated at P/P_o = 0.95; [c]Pore diameters were estimated from the adsorption branch of the nitrogen isotherm using the BJH method.

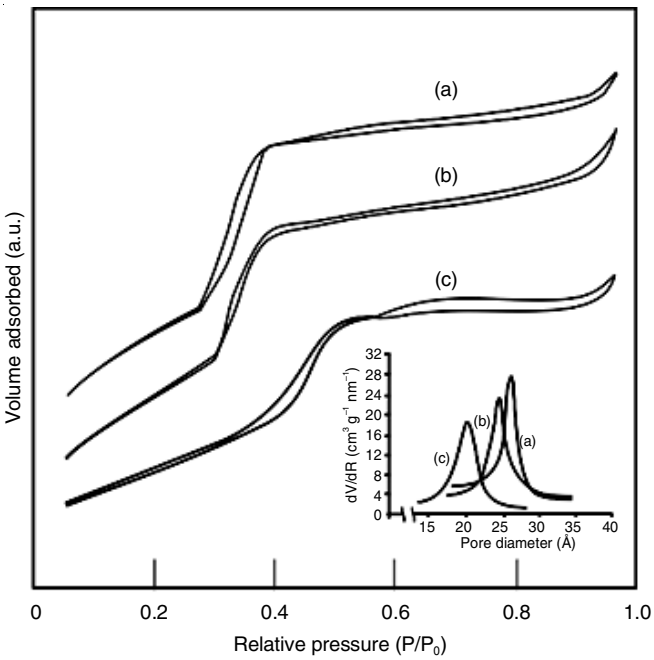

Fig. 9. N_2-physisorption isotherms of cal-RH-MCM-48 (a), silyl-RH-MCM-48 (b) and Fe_2O_3(0.10M,4h,60°C)@silyl-RH-MCM-48 (c). The inset shows the pore size distribution

cal-RH-MCM-48 (Fig. 9a) and silyl-RH-MCM-48 (Fig. 9b), showing that modification of the outer surface with TMCS does not change the texture characteristics of the material. This is understandable to consider that the silylation has been carried out on the outer surface only, hence it does not affect the porosity. This isotherm profile fits the type IV isotherm of the IUPAC nomenclature, which is characteristic of mesoporous materials [43]. An increase in isotherm curves at $P/P_o < 0.3$ is due to the adsorption of the single layer of N_2 on the mesoporous walls, while the steep increase around $0.3 < P/P_o < 0.38$ is referred to the capillary condensation in the pore of RH-MCM-48.

The sharpness of the capillary condensation steps in these isotherms is due to the uniformity of pores and their narrow size distribution. The high slope of the curve in the capillary condensation stage of these isotherms is due to the presence of relatively uniform pores, *i.e.* with a narrow size distribution. These results are in accordance with the XRD patterns (Fig. 2b-c), exhibiting well-resolved secondary diffraction above $2\theta = 3.5°$ ([232] peak), indicating a highly long-range order of these materials. These isotherms exhibiting the type H1 hysteresis loop, generally correspond to the capillary condensation in the mesopores and are typical of mesoporous materials [43]. The long plateau at higher relative pressures indicates the occurrence of multilayer adsorption after capillary condensation on the surface of the material. The narrow H4 type hysteresis loop which emerges at $0.40 < P/P_o < 1.00$ indicates the narrow range of pore sizes contained in the material. Finally, at P/P_o close to 1, the isotherm curves increase again which caused by the filling of gas in the interparticle space [56]. These results suggested that the external silylation treatment does not alter the ordered structure of RH-MCM-48 significantly, which is consistent with the X-ray diffractogram data.

In case of Fe_2O_3(0.10M,4h,60°C)@silyl-RH-MCM-48 sample (Fig. 9c), the isotherm still displays type IV. The condensation step is sharp enough at P/P_o of around 0.3, however it is less sharp as compared to those of both cal-RH-MCM-48 and silyl-RH-MCM-48 samples. In addition, the step inflection point slightly shifts to a higher relative pressure (Fig. 9c). These observations indicated that the impregnation of Fe^{3+} has reduced the ordered structure of RH-MCM-48 and the uniformity of pore channels. This phenomenon may be caused by the isomorphic substitution of Si^{4+} in the skeleton by Fe^{3+}, which is in good agreement with the data of X-ray diffractograms and FTIR spectra. Similar results has also been reported by few researchers [43,57].

Table-4 exhibits that there is almost no difference between the cal-RH-MCM-48 and silyl-RH-MCM-48 samples in terms of surface area, pore-volume and pore diameter. However, Fe_2O_3(0.10M,4h,60°C)@silyl-RH-MCM-48 sample shows a remarkable decrease in all parameter compared to the other two samples. This decrease may be caused by the filling of iron oxide nanoparticles in the pores.

TEM studies: Fig. 10a exhibits various sizes (100-300 nm) of spherical cal-RH-MCM-48 particles formed in lower magnification, while Fig. 10b in higher magnification. The spherical shape of MCM-48 particles has also reported by Qian *et al*. [43]. The ordered cubic arrays of the mesoporous framework is confirmed (Fig. 10c), when the electron beam is perpendicular to the pore axis (Fig. 10d), when the electron beam is parallel to the pore axis.

These images show a highly ordered mesostructure and well-developed mesopores. It was clear that the pore structure was regular over the whole particle, indicating the formation of a well-defined ordered mesoporous structure of MCM-48. These results matched perfectly with the characterization data of XRD diffractogram and N_2 sorption isotherms. Based on the images (Fig. 10), the pore sizes were found to be about 2.5 nm in diameter and 0.7 nm in wall thickness.

DR-UV-vis spectra analysis: The DR-UV-vis spectrum of Fe_2O_3(0.10M,4h,60°C)@silyl-RH-MCM-48 is presented in Fig. 11a. For the purpose of comparison, the spectrum of the bulk Fe_2O_3 (Fig. 11b) is also presented. It is clear that Fe_2O_3

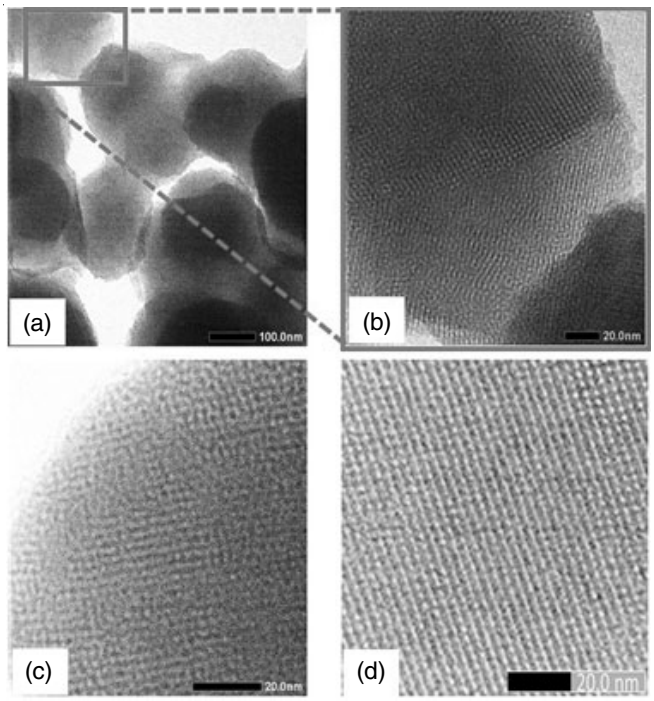

Fig. 10. TEM images of cal-RH-MCM-48: low magnification (a), medium magnification (b), high magnification with the electron beam was perpendicular to the pore axis (c) and high magnification with the electron beam was parallel to the pore axis (d)

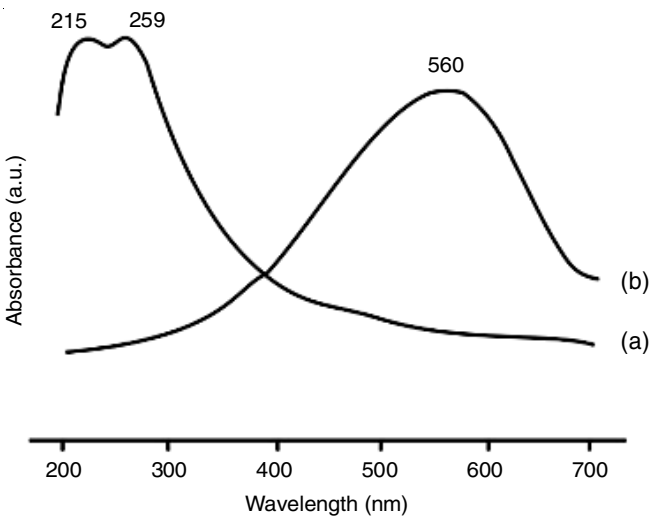

Fig. 11. DR-UV-vis spectrum of Fe_2O_3(0.10M,4h,60ºC)@silyl-RH-MCM-48 (a) and bulk = γ-Fe_2O_3 (b)

bulk sample shows broad band with strong maxima at 560 nm, originating from all possible *d-d* transitions [58].

On the other hand, Fe_2O_3(0.10M,4h,60ºC)@silyl-RH-MCM-48 sample exhibits two absorption peaks at the smaller wavelengths, *i.e.* at 215 and 259 nm. This blue shift is caused by the transformation of particle size from bulk to the molecular size, known as the quantum size effect, that happen to iron oxide nanoparticles in mesoporous [59]. This interpretation matches well with the characterization data obtained from both FTIR spectra and the N_2 sorption isotherms. The peaks at 215 and 259 nm are attributed to the ligand-to-metal charge transfer (LMCT) transitions involving the isolated framework of Fe^{3+} in $(FeO)^{-4}$ tetrahedral geometry. This transition belongs to the electronic transition of O^{2-} to the t_{2g} and e_g orbitals of Fe^{3+}, respectively, in the network structure [60]. This interpretation agrees very well with the presence of isomorphic substitution of Si^{4+} by Fe^{3+} as illustrated in Fig. 5.

It is interesting to observe that in Fig. 10a has no absorption above 350 nm, indicating that the sample is free of bulky iron oxide and/or oxyhydroxides on the outer surface [26,61]. Also, the colour of sample is white, suggesting that there are no bulky iron oxides. These results are easily understandable since the external silanol group has been inactivated by the hydrophobic trimethylsilyl group. It seems that trimethylsilyl group acts effectively as a deactivator so that Fe^{3+} ions cannot interact with the deactivated silanol groups *via* hydrogen bond, which is the initial step in the formation of iron oxides. Meanwhile, some researchers [62-64] have also reported the similar observations. This is quite understandable since they have used unsilylated mesoporous silicates as a host material so that the formation of iron oxides is not protected.

EPR spectra analysis: Fig. 12 shows the EPR spectrum of Fe_2O_3(0.10M,4h,60ºC)@silyl-RH-MCM-48 recorded at room temperature. This spectrum exhibits three different peaks emerging at various g_e values (4.3, 2.2 and 1.9), suggesting the presence of three different environments around the trivalent iron. The weak peak at g = 4.3 proves the presence of Fe in the skeleton and is characteristic for the paramagnetic Fe^{3+} cations isolated in strong rhombic distorted tetrahedral coordination [26,65]. The strong peak centered at 2.2 is attributed to non-framework (superparamagnetic) iron hydroxides/oxide nanoparticles located in the pores [26,65]. The rather strong peak at 1.9 is attributed to the extra-framework of Fe^{3+} or trivalent iron framework (Fe^{3+} species in octahedral coordination) [26]. Both DR-UV-Vis and EPR spectra also suggested that the loading of trivalent iron in mesoporous matrix gives rise not only to the iron oxide nanoparticles dispersed in the pores, but also to the isomorphic substitution of Fe^{3+} in the framework sites of Silyl-RH-MCM-48 structures.

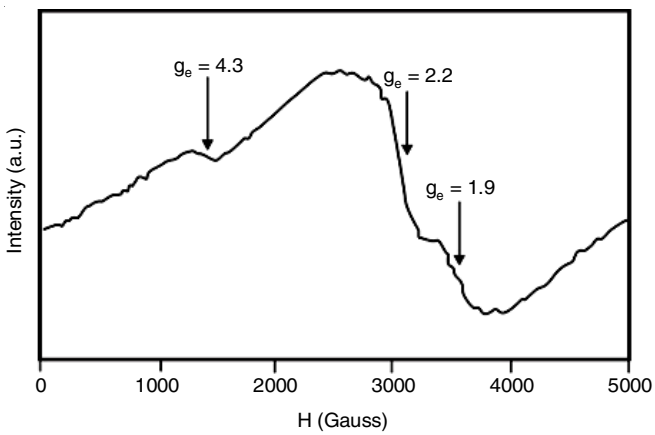

Fig. 12. EPR spectrum of Fe_2O_3(0.10M,4h,60°C)@silyl-RH-MCM-48

VSM curve: The magnetization curve of Fe_2O_3(0.10M, 4h,60ºC)@silyl-RH-MCM-48 recorded on VSM at room temperature is shown in Fig. 13. This magnetization curve shows the absence of hysteresis, meaning that the composite exhibits

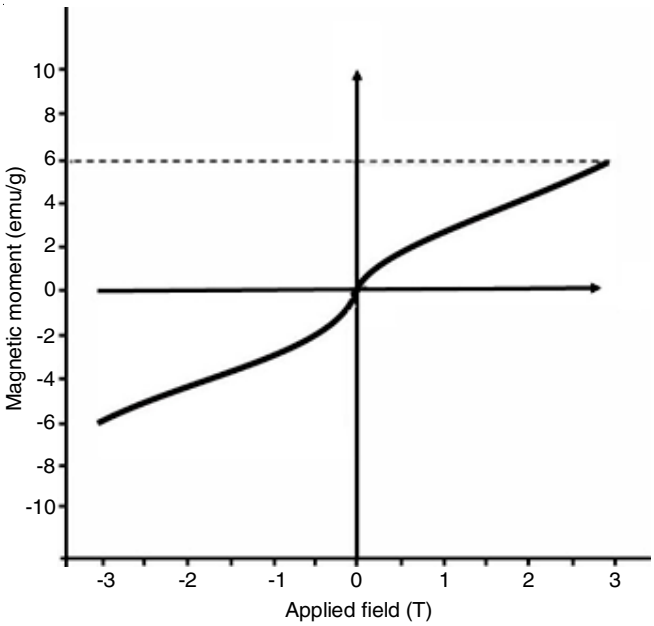

Fig. 13. Room temperature magnetization curves for Fe_2O_3(0.10M,4h, 60°C)@silyl-RH-MCM-48

superparamagnetic behaviour at room temperature. Similar finding has also been reported by several workers [26-28]. This superparamagnetic behaviour is believed to be originated from the γ-Fe_2O_3 nanoparticles formed in the silyl-RH-MCM-48 host pore. As shown in Fig. 13, an increase in the external magnetic field up to 3T results in the increase in magnetization up to 6 emu only without any saturation. This very low magnetization (compared to 76 emu/g for bulky γ-Fe_2O_3) is probably due to the spin canting resulted from the discontinuity of the super-exchange bonds between the Fe cations [66].

Fig. 13 also shows that remanence (M_r) and coercivity (H_c) are zero. Compared with the bulk of γ-Fe_2O_3 (M_r = 63 emu/g and H_c = 250-400 G), the absence of remanence and coercivity in this curve can be attributed to the single magnetic domain cluster bearing to nanocomposite. For bulky systems, the coercivity is related to the motion of the magnetic domain walls in the presence of a magnetic field; whereas in single-domain particles, coercivity comes from the magnetization rotation away from the easy axis [66].

The superparamagnetic materials can be attracted to the magnetic field but there will be no more attraction between the particles after the field being removed, therefore this materials have great potential to be used for several applications. Also, the Brownian rotation phenomenon and Ne´el relaxation mechanism, which have implications for the ability of superparamagnetic nanoparticles to transmit heat in an alternating magnetic field can be exploited for cancer treatment when it reaches hyperthermic temperatures [41].

Conclusion

Rice husk silica synthesis of MCM-48 (RH-MCM-48) with an ordered *Ia3d* cubic mesostructure has been successfully synthesized by the sonochemical method using rice husk as a source of silica. The products are spherical particles of varying sizes (100-450 nm) with regular mesopores and a narrow pore size distribution. The BET surface area, pore-volume and BJH pore diameter were 984.28 m^2/g, 0.763 × 10^{-6} m^3/g and 2.589 nm, respectively. The success of deactivation using trimethylchlorosilane (TMCS) on the outer silanol group of RH-MCM-48 to produce silyl-RH-MCM-48 has been confirmed by FTIR spectra. The optimal conditions for impregnation of Fe^{3+} into the silyl-RH-MCM-48 pore system are Fe^{3+} concentration of 0.1 M, contact time of 4 h and mixing temperature of 60 ºC. The FTIR spectra, DR-UV-visible spectra, EPR spectra and magnetization curve have suggested the formation of superparamagnetic iron oxide nanoparticles in the pore system and the occurrence of partial isomorphic substitution of Si^{4+} in the skeleton by Fe^{3+}. In addition, it has been interestingly found that the external silylation is able to prevent the formation of bulky iron oxides on the outer surface of MCM-48 host.

ACKNOWLEDGEMENTS

The authors are grateful to the Directorate General of High Education (DGHE), Ministry of Education, Culture, Research and Technology, Republic of Indonesia for financial support through research grant managed by Universitas Gadjah Mada.

CONFLICT OF INTEREST

The authors declare that there is no conflict of interests regarding the publication of this article.

REFERENCES

1. B. Duong, H. Khurshid, P. Gangopadhyay, J. Devkota, K. Stojak, H. Srikanth, L. Tetard, R.A. Norwood, N. Peyghambarian, M.H. Phan and J. Thomas, *Nano-Micro Small*, **10**, 2840 (2014) https://doi.org/10.1002/smll.201303809
2. T. Das, I.W. Nah, J.G. Choi and I.-H. Oh, *React. Kinet. Mech. Catal.*, **118**, 669 (2016); https://doi.org/10.1007/s11144-016-1035-4
3. S.L. Iconaru, R. Guégan, C.L. Popa, M. Motelica-Heino, C.S. Ciobanu and D. Predoi, *Appl. Clay Sci.*, **134**, 128 (2016); https://doi.org/10.1016/j.clay.2016.08.019
4. S.M. Dadfar, K. Roemhild, N.I. Drude, S. von Stillfried, R. Knüchel, F. Kiessling and T. Lammers, *Adv. Drug Deliv. Rev.*, **138**, 302 (2019); https://doi.org/10.1016/j.addr.2019.01.005
5. E. Chamorro, M.J. Tenorio, L. Calvo, M.J. Torralvo, R. Sáez-Puche and A. Cabañas, *J. Supercrit. Fluids*, **159**, 104775 (2020); https://doi.org/10.1016/j.supflu.2020.104775
6. Wahajuddin and S. Arora, *Int. J. Nanomedicine*, 3445 (2012); https://doi.org/10.2147/IJN.S30320
7. D. Pan, A.H. Schmieder, S.A. Wickline and G.M. Lanza, *Tetrahedron*, **67**, 8431 (2011); https://doi.org/10.1016/j.tet.2011.07.076
8. V.C. Pierre, M.J. Allen and P. Caravan, *J. Biol. Inorg. Chem.*, **19**, 127 (2014); https://doi.org/10.1007/s00775-013-1074-5
9. J. Dulinska-Litewka, A. Lazarczyk, P. Halubiec, O. Szafranski, K. Karnas and A. Karewicz, *Materials*, **12**, 617 (2019); https://doi.org/10.3390/ma12040617
10. S. Uthaman, S.J. Lee, K. Cherukula, C.S. Cho and I.K. Park, *BioMed Res. Int.*, **2015**, 959175 (2015); https://doi.org/10.1155/2015/959175
11. D.H. Nguyen, J.S. Lee, J.H. Choi, K.M. Park, Y. Lee and K.D. Park, *Acta Biomater.*, **35**, 109 (2016); https://doi.org/10.1016/j.actbio.2016.02.020
12. X. Song, G. Yan, S. Quan, E. Jin, J. Quan and G. Jin, *Biosci. Biotechnol. Biochem.*, **83**, 622 (2019); https://doi.org/10.1080/09168451.2018.1562875

13. F. Tang, L. Li and D. Chen, *Adv. Mater.*, **24**, 1504 (2012); https://doi.org/10.1002/adma.201104763
14. X. Chen, X. Cheng, A.H. Soeriyadi, S.M. Sagnella, X. Lu, J.A. Scott, S.B. Lowe, M. Kavallaris and J.J. Gooding, *Biomater. Sci.*, **2**, 121 (2014); https://doi.org/10.1039/C3BM60148J
15. V. Palos-Barba, A. Moreno-Martell, V. Hernández-Morales, C.L. Peza-Ledesma, E.M. Rivera-Muñoz, R. Nava and B. Pawelec, *Materials*, **13**, 927 (2020); https://doi.org/10.3390/ma13040927
16. V. Rizzi, J. Gubitosa, P. Fini, S. Nuzzo and P. Cosma, *Sustain. Mater. Technol.*, **26**, e00231 (2020); https://doi.org/10.1016/j.susmat.2020.e00231
17. M. Ebrahimi-Gatkash, H. Younesi, A. Shahbazi and A. Heidari, *Appl. Water Sci.*, **7**, 1887 (2017); https://doi.org/10.1007/s13201-015-0364-1
18. A. Shahbazi, H. Younesi and A. Badiei, *Can. J. Chem. Eng.*, **91**, 739 (2013); https://doi.org/10.1002/cjce.21691
19. F. Sahel, F. Sebih, S. Bellahouel, A. Bengueddach and R. Hamacha, *Res. Chem. Intermed.*, **46**, 133 (2020); https://doi.org/10.1007/s11164-019-03939-5
20. T. Tamoradi, M. Ghadermazi and A. Ghorbani-Choghamarani, *J. Saudi Chem. Soc.*, **23**, 846 (2019); https://doi.org/10.1016/j.jscs.2019.02.003
21. E. Karakhanov, A. Akopyan, O. Golubev, A. Anisimov, A. Glotov, A. Vutolkina and A. Maximov, *ACS Omega*, **4**, 12736 (2019); https://doi.org/10.1021/acsomega.9b01819
22. A. Fernandez-Fernandez, R. Manchanda and A. McGoron, *Appl. Biochem. Biotechnol.*, **165**, 1628 (2011); https://doi.org/10.1007/s12010-011-9383-z
23. J. M. Rosenholm, C. Sahlgren and M. Linden, *Curr. Drug Targets*, **12**, 1166 (2011); https://doi.org/10.2174/138945011795906624
24. A. Baeza, M. Colilla and M. Vallet-Regí, *Expert Opin. Drug Deliv.*, **12**, 319 (2015); https://doi.org/10.1517/17425247.2014.953051
25. M. Popova, N. Koseva, I. Trendafilova, H. Lazarova, V. Mitova, J. Mihály, D. Momekova, G. Momekov, I.Z. Koleva, H.A. Aleksandrov, G.N. Vayssilov and Á. Szegedi, *Molecules*, **25**, 5129 (2020); https://doi.org/10.3390/molecules25215129
26. S.E. Dapurkar and P. Selvam, *Mater. Phys. Mech.*, **4**, 13 (2001).
27. S. Huang, C. Li, Z. Cheng, Y. Fan, P. Yang, C. Zhang, K. Yang and J. Lin, *J. Colloid Interface Sci.*, **376**, 312 (2012); https://doi.org/10.1016/j.jcis.2012.02.031
28. X. Zang and W. Xie, *J. Oleo Sci.*, **63**, 1027 (2014); https://doi.org/10.5650/jos.ess14089
29. L. Li, X. Wang, D. Zhang, R. Guo and X. Du, *Appl. Surf. Sci.*, **328**, 26 (2015); https://doi.org/10.1016/j.apsusc.2014.11.116
30. J. Liu, S. Fang, R. Jian, F. Wu and P. Jian, *Powder Technol.*, **329**, 19 (2018); https://doi.org/10.1016/j.powtec.2018.01.066
31. L.C. Guan, Ph.D. Thesis, Mesoporous MCM-48 Synthesized from Rice Husk Ash Silica: Physico-chemical Properties and its Catalytic Activity in Acylation Reaction, Faculty of Science Universiti Teknologi Malaysia (2005).
32. H. Wang, W. Qian, J. Chen, Y. Wu, X. Xu, J. Wang and Y. Kong, *RSC Adv.*, **4**, 50832 (2014); https://doi.org/10.1039/C4RA08333D
33. A. Popat, J. Liu, Q. Hu, M. Kennedy, B. Peters, G.Q. Lu and S.Z. Qiao, *Nanoscale*, **4**, 970 (2012); https://doi.org/10.1039/C2NR11691J
34. W. Zhao, M. Qin, L.N. Wang, J.L. Chu, J.K. Qu, S.H. Li, Q.Z. Li and T. Qi, *J. Colloid Interface Sci.*, **384**, 81 (2012); https://doi.org/10.1016/j.jcis.2012.05.057
35. D. Battegazzore, S. Bocchini, J. Alongi and A. Frache, *RSC Adv.*, **4**, 54703 (2014); https://doi.org/10.1039/C4RA05991C
36. R.M. Mohamed, I.A. Mkhalid and M.A. Barakat, *Arab. J. Chem.*, **8**, 48 (2015); https://doi.org/10.1016/j.arabjc.2012.12.013
37. N.K. Renuka, A.K. Praveena and K. Anas, *Mater. Lett.*, **70**, 109 (2013); https://doi.org/10.1016/j.matlet.2013.07.074
38. M. Bhagiyalakshmi, L.J. Yun, R. Anuradha and H.T. Jang, *J. Hazard. Mater.*, **175**, 928 (2010); https://doi.org/10.1016/j.jhazmat.2009.10.097
39. U. Gedikli, Z. Misirlioglu, P.A. Bozkurt and M. Canel, *J. Turkish Chem. Soc.*, **2**, 54 (2015).
40. T.M. Salem Attia, X.L. Hu and D.Q. Yin, *J. Exp. Nanosci.*, **9**, 551 (2014); https://doi.org/10.1080/17458080.2012.677549
41. S. Huang, Y. Fan, Z. Cheng, D. Kong, P. Yang, Z. Quan, C. Zhang and J. Lin, *J. Phys. Chem. C*, **113**, 1775 (2009); https://doi.org/10.1021/jp808886c
42. G. Lente and I. Fábián, *Inorg. Chem.*, **38**, 603 (1999); https://doi.org/10.1021/ic980813c
43. W. Qian, H. Wang, J. Chen and Y. Kong, *Materials*, **8**, 1752 (2015); https://doi.org/10.3390/ma8041752
44. N.Y. He, J.M. Cao, S.L. Bao and Q.H. Xu, *Mater. Lett.*, **31**, 133 (1997); https://doi.org/10.1016/S0167-577X(96)00258-3
45. L. Pasqua, F. Testa, R. Aiello, F. Di Renzo and F. Fajula, *Micropor. Mesopor. Mater.*, **44-45**, 111 (2001); https://doi.org/10.1016/S1387-1811(01)00174-3
46. H. Yang, G. Zhang, X. Hong and Y. Zhu, *Micropor. Mesopor. Mater.*, **68**, 119 (2004); https://doi.org/10.1016/j.micromeso.2003.12.014
47. S.I. Karpov, F. Roessner, V.F. Selemenev, N.A. Belanova and O.O. Krizhanovskaya, *Russ. J. Phys. Chem.*, **87**, 1888 (2013); https://doi.org/10.1134/S0036024413110125
48. X.S. Zhao, G.Q. Lu and G.J. Millar, *Ind. Eng. Chem. Res.*, **35**, 2075 (1996); https://doi.org/10.1021/ie950702a
49. W. Lutz, *Adv. Mater. Sci. Eng.*, **2014**, 724248 (2014); https://doi.org/10.1155/2014/724248
50. M.D. Brankovic, A.R. Zarubica, T.D. Andjelkovic and D.H. Andjelkovic, *Adv. Technol.*, **6**, 50 (2017); https://doi.org/10.5937/savteh1701050B
51. P.E.G. Casillas, C.A.R. Gonzalez and C.A.M. Pérez, Infrared Spectroscopy of Functionalized Magnetic Nanoparticles; In: Infrared Spectroscopy, Intech Open, London, p. 21 (2012).
52. N.I. Taib, S. Endud and M.N. Katun, *Int. J. Chem.*, **3**, 2 (2011); https://doi.org/10.5539/ijc.v3n3p2
53. R.M. Cornell and U. Schwertmann, The Iron Oxides, John Wiley & Sons, New York, Ed.: 2, p. 146 (2003).
54. B.B. Zviagina, V.A. Drits and O.V. Dorzhieva, *Minerals*, **10**, 153 (2020); https://doi.org/10.3390/min10020153
55. D.V. Quy, N.M. Hieu, P.T. Tra, N.H. Nam, N.H. Hai, N. Thai Son, P.T. Nghia, N.T.V. Anh, T.T. Hong and N.H. Luong, *J. Nanomater.*, **2013**, 603940 (2013); https://doi.org/10.1155/2013/603940
56. S.J. Gregg and K.S.W. Sing, Adsorption, Surface Area and Porosity, Academic Press: New York, p. 49 (1992).
57. R. Longloilert, T. Chaisuwan, A. Luengnaruemitchai and S. Wongkasemjit, *J. Sol-Gel Sci. Technol.*, **61**, 133 (2012); https://doi.org/10.1007/s10971-011-2602-9
58. H. Xin, J. Liu, F. Fan, Z. Feng, G. Jia, Q. Yang and C. Li, *Micropor. Mesopor. Mater.*, **113**, 231 (2008); https://doi.org/10.1016/j.micromeso.2007.11.022
59. M. Iwamoto, T. Abe and Y. Tachibana, *J. Mol. Catal. A*, **155**, 143 (2000); https://doi.org/10.1016/S1381-1169(99)00330-1
60. A.I. Carrillo, E. Serrano, R. Luque and J. García-Martínez, *Appl. Catal. A Gen.*, **453**, 383 (2013); https://doi.org/10.1016/j.apcata.2012.12.041
61. Y. Li, Z.C. Feng, Y.X. Lian, K.Q. Sun, L. Zhang, G.Q. Jia, Q.H. Yang and C. Li, *Micropor. Mesopor. Mater.*, **84**, 41 (2005); https://doi.org/10.1016/j.micromeso.2005.05.021
62. A. Tuel, I. Arcon and J.M.M. Millet, *J. Chem. Soc.*, **94**, 3501 (1998); https://doi.org/10.1039/A806912C
63. A. Bhaumik, S. Samanta and N.K. Mal, *Pramana –J. Phys.*, **65**, 5 (2005).
64. D.Q. Khieu, D.T. Quang, T.D. Lam, N.H. Phu, J.H. Lee and J.S. Kim, *J. Incl. Phenom. Macrocycl. Chem.*, **65**, 73 (2009); https://doi.org/10.1007/s10847-009-9624-8
65. W. Thitsartarn, E. Gulari and S. Wongkasemjit, *Appl. Organomet. Chem.*, **22**, 97 (2008); https://doi.org/10.1002/aoc.1356
66. L. Zhang, G.C. Papaefthymiou and J.Y. Ying, *J. Phys. Chem. B*, **105**, 7414 (2001); https://doi.org/10.1021/jp010174i